

Polarization Plasticity of Ferroelectric Nematics: a case of Electrostatic Frustration in Simple Planar Electrode Cells

Stefano Marni^{1,X}, Federico Caimi^{1,X,*}, Luca Casiraghi¹, Jordan Hobbs², Calum J. Gibb³, Richard Mandle^{2,3}, Giovanni Nava¹, Tommaso Bellini^{1,*}

**1 Affiliation: Medical Biotechnology and Translational Medicine
Department, University of Milan, 20133, Milano, Italy**

**2 Affiliation: School of Physics and Astronomy, University of Leeds, Leeds,
UK, LS2 9JT**

3 School of Chemistry, University of Leeds, Leeds, UK, LS2 9JT

X equally contributed.

*** federico.caimi@unimi.it, tommaso.bellini@unimi.it**

Abstract

Because of their spontaneous bulk polarization, ferroelectric nematic liquid crystals can be easily brought by surface coupling or confinement in a state in which the accumulation of bound charges becomes incompatible with polar order, creating frustration. This condition also occurs in the simplest cells with parallel uncoated metal electrodes where we find that the polarization charge accumulating on the electrodes is proportional to the applied voltage for $\Delta V < V_{sat}$, a threshold value independent of cell thickness. We show that below V_{sat} , frustration drives the system into a regime of polarization plasticity, in which nematic ordering is preserved and the nematic director remains perpendicular to the electrodes, while instead the polarization is reduced to cancel the internal electric field. In this regime, the kinetics of bound charge reversal becomes independent from ΔV . The observations are consistent with a model in which the system splits into antipolar tubular domains of mesoscale diameter extending from electrode to electrode, in which the polarization retains its unconstrained equilibrium value, separated by pure polarization-reversal walls.

Introduction

Spontaneous polar order is a striking form of collective organization in condensed matter. While ferroic order has been studied for over a century in 3D ferroelectric and ferromagnetic crystals and for decades in 1D crystals (the ferroelectric Smectic C* phase), the recent discovery of the ferroelectric nematic (N_F) phase [1–4] has opened the new frontier of a fully liquid material with macroscopic polarization. Freed from crystal periodicity constraints, the polar ordering in N_F is uncoupled from any specific direction in the 3D space. Thus, unlike all other ferroic materials, N_F cannot self-sustain depolarization field in any significant proportion, a property that makes N_F behave remarkably differently from ordinary nematic Liquid Crystals (LCs). A key manifestation of this difference is the behavior of N_F in contact with solid surfaces.

The presence of a spontaneous polarization implies that bound charges accumulate on any surface not parallel to P . Because polar ordering in the N_F phase involves

nearly all molecules [1], any component of \vec{P} normal to confining dielectric walls produces a large surface charge density $\sigma_b = \vec{P} \cdot \hat{n}$, which in turn generates strong uncompensated depolarization fields. In solid ferroelectric and ferromagnetic materials, and to some extent also Smectic C*, polarity is preserved even in the presence of adverse fields. In contrast, because of its fluidity, N_F fluid responds to any internal electric field through local or global reorientation of \vec{P} , until the fields are suppressed.

A clear manifestation of this behavior is the cancellation of electric-field components perpendicular to N_F -dielectric interfaces. This phenomenon, which we previously termed “ferroelectric superscreening,” makes N_F phases extremely sensitive to confinement geometry and enables the guiding of polarization and electric fields along curved micro-channels [5]. In other dielectric-bounded geometries, such as droplets squeezed between parallel glass plates, interfacial charge accumulation is mitigated by the formation of in-plane striped domains with antiparallel \vec{P} [1, 6, 7], by twisting along the z axis [8], and by rotations of \vec{P} near the droplet boundaries [7] or around air bubble inclusions [1]. As a result, a uniform polar alignment is rarely observed.

Quite different is the behavior of N_F when in contact with the metal surfaces of electrodes. In this case, σ_b is mirrored in the electrode by an equivalent amount of free charges $\sigma_e \approx \sigma_b$. The large value of σ_b makes the presence of any even tiny separation gap δ between the planes of bound and free charges a key element affecting voltages and electric fields applied on N_F . Indeed, with $\sigma_b \approx 5 \mu\text{C}/\text{cm}^2$ and $\delta \approx 1 \text{ nm}$, the voltage drop V_I relative to the insulating layer between electrode and material becomes $V_I \approx \sigma_b \epsilon_0 / \delta \approx 2V$, a quantity comparable with the minimum applied voltage in many studies of N_F [9–11]. Although such experimental situations were investigated on ferroelectric smectics in the 90s [12], early studies on N_F didn’t include V_I in the analysis since in conventional nematics this quantity can be neglected. The relevance of V_I was pointed out [13] and included in the most recent dielectric studies [14, 15]. Voltage drop at the electrodes has also been recently recognized as the cause of negative capacitance observed in thin N_F sandwich electrode cells [16].

For each electrode, V_I is maximized when the polar axis is normal to the electrode, reaching a limit value of $V_I^{max} = P\epsilon_0/\delta$. This means that when the applied voltage ΔV is $\Delta V = V_{sat} = 2V_I^{max}$, the entire voltage drops in the vicinity of the electrodes, with \vec{P} and optical axis oriented perpendicular to the electrodes and negligible internal electric field \vec{E}_{NF} . When $\Delta V < V_{sat}$, a frustrating condition is realized since in this condition maintaining \vec{P} aligned perpendicular to the electrodes would lead to a \vec{E}_{NF} parallel and opposite to \vec{P} . The “polarization external capacitance Goldstone” (PCG) reorientation mode introduced in Ref. [13] solves the problem by assuming that \vec{P} rotates away from the normal to the electrodes, thus lowering σ_b until \vec{E}_{NF} is canceled and thus compatible with the orientation of \vec{P} . While this compensation mechanism can possibly describe the N_F behavior in some thin cells, it cannot be general since rotation implies depositing charges on the lateral dielectric walls of the cell, generating strong uncompensated fields. At the same time, the splitting of the phase into micro-domains undergoing incoherent rotations around distinct axes would also result in local accumulation of charge and thus large local fields, a condition maybe acceptable as a transient state but not as the equilibrium state when $\Delta V < V_{sat}$.

In the absence of apparent solutions to these frustrating conditions of conflicting polar order and depolarizing field, and since the condition $\Delta V < V_{sat}$ is of general relevance in studies and application of N_F phases, we performed electrical and optical (linear and nonlinear) experiments in this regime in planar parallel electrode cells with thicknesses ranging from tenth of microns to millimeters. We find that the N_F phase can enter a regime of ‘Polarization Plasticity’, which we introduce here, in which the effective polarization self-adjusts to cancel the internal electric field while preserving nematic order. The equilibrium and kinetic behavior indicate that the plasticity is

achieved through the splitting of the system in tubular domains of opposite polarity connected by pure polarization-reversal walls [4], a configuration that in the language of classical ferroics would correspond to elongated Weiss domains bounded by Ising-like walls and spanning the cell thickness [4].

Results

In this work we explored a variety of cells belonging to two families (see Table 1): bulky (B) cells, having sizes in the mm range in all three dimensions and bare stainless steel electrodes, enabling accurate charge measurements, and optical (O) thin cells with in-plane switching type electrodes of different materials for characterization by bright-field and polarized transmission microscopy, Second Harmonic Generation (SHG) and also, in the thickest O-cell, charge measurements. Cells were filled with DIO, synthesized as in Ref. [17] whose N_F phase is in the temperature interval $44^\circ C < T < 69^\circ C$ [2]. All experiments have been performed at $T \approx 60^\circ C$. Further details on cells preparation are reported in the Materials and Methods section.

Table 1. Bulky (B) and Optical thin (O) used in this study d: electrode distance; h: cell height; w: electrode length; S: electrode surface.

#	d (mm)	h(mm)	w(mm)	S=hw (mm ²)	Electrodes
B1	0.8	2.4	2.0	4.8	stainless steel
B2	1.1	1.0	2.0	2.0	stainless steel
B3	2.2	1.4	2.0	2.8	stainless steel
B4	4.0	2.2	2.0	4.4	stainless steel
O1	3.0	$35 \cdot 10^{-3}$	10	0.35	stainless steel
O2	3.0	$20 \cdot 10^{-3}$	10	0.2	aluminum
O3	3.0	$11 \cdot 10^{-3}$	15	0.17	ITO

Equilibrium Properties: Polarization Charges on the Electrodes

We measured, via polarization-reversal experiments, the polarization charge deposited by the N_F material on the surfaces of the cell electrodes. Measurements are performed by connecting a voltage generator, supplying a square wave of amplitude ΔV , to the cells in series with a probe resistance R (see Fig. 1a). Figure 1b shows typical $i(t)$ (red lines) flowing after ΔV reversal (black lines). The frequency of the square waves was chosen to allow the system to reach equilibrium ($i \approx 0$). Integration of $i(t)$ yields the total variation of surface bound charge $Q = 2\sigma_e S$ due to polarization reversal (Fig. 1c), where S is the electrode area.

The surface charge density obtained from the voltage-reversal curves is shown in Fig. 1c–d as a function of the applied voltage ΔV , for bulky cells with different electrode separations d . For $\Delta V > 10$ V, we obtain $\sigma_b = 4.6 \mu C/cm^2$, consistent with the value of P for DIO reported in the literature [2]. We interpret the small drift of σ_b with ΔV , captured by the slope of the dashed magenta line, as an experimental artifact.

Upon decreasing ΔV below 10V (Fig. 1d), σ_b decreases in all cells, with nearly identical values, toward $\sigma_b = 0$ for $\Delta V = 0$. In particular, at low voltages, a clean linear dependence of σ_b on ΔV is observed (brown dashed line), corresponding to a capacitance $C_{eff}/S = 1.2 \mu C/(V \cdot cm^2)$ independent from d . This finding supports the notion that two insulating layers are present between the polar fluid and the electrodes,

as proposed in Ref. [13]. $V_{sat} = 3.7V$ obtained from the intersection of the two linear fits of σ_b vs. ΔV at the large and small ΔV marks the crossover between two regimes (pink vs. blue shadings). A similar $P(\Delta V)$ behavior was observed by Nikolova et al. [10] using a different cell geometry and material. Their crossover value ($\approx 2.5V$) is compatible with our measured V_{sat} .

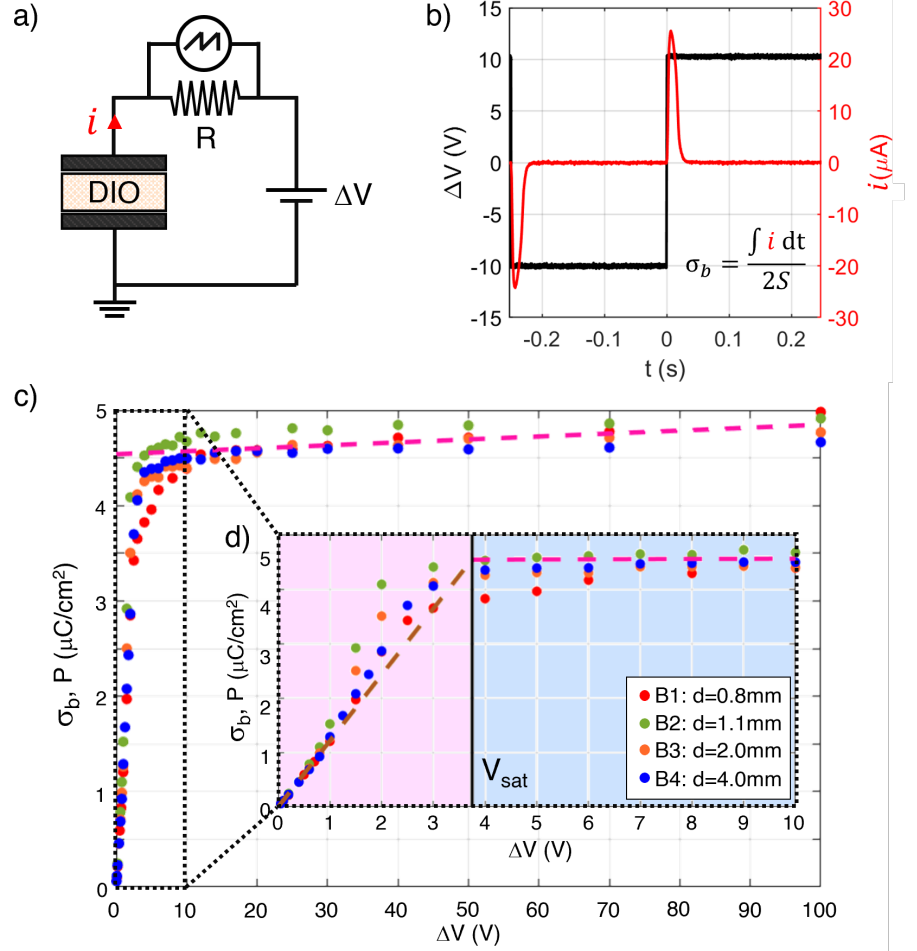


Figure 1. Charge measurements a) Electrical scheme used for the measurement of the current intensity i following voltage reversal. b) Typical $i(t)$ profile (red line, right-hand axis) recorded when applying a squared wave voltage (black curve, left-hand axis). c) Polarization charge density σ_b (generally coinciding with P , see text) as a function of the applied voltage ΔV in bulky cells differing in electrode separation d . d) Expansion of the low voltage region of panel c. V_{sat} , marking the crossover between Polarization Plasticity (pink shading) and homogeneous N_F polarization (blue shading) is obtained by the intersection of the two linear lines fit at low voltages (0-1V, brown dashed line) and high voltages (10-100V, magenta dashed line).

Equilibrium Properties: Birefringence and Second Harmonic Generation

To better explore the linear decrease of σ_b in the low voltage regime, we repeated the charge measurements in the thin cells, to enable the comparison between electrical and optical observations. Although the data are much noisier, the $\sigma_b(\Delta V)$ behavior remains the same as in bulky cells, but with a different V_{sat} , indicating a dependence on geometry and electrode material. Data for the O3 cell are shown in Fig. 2a (black dots). All data sets in the figure are normalized to their value at large ΔV to allow comparisons.

Fig. 2b shows three transmission microscope images of the O3 cell through crossed polarizers. We find that at very low voltages ($\Delta V < V_{dis} \approx 0.5V$ - gray shaded region) the cell develops irregular textures and color indicating the presence of twisted structures and domain walls. For $\Delta V > V_{dis}$ the cell takes the appearance of a standard homogeneous nematic with some minor granularity that disappears as ΔV increases.

In the same cell we measured the optical birefringence Δn with a Berek compensator, which we plot in Fig. 2a (dark red dots). In line with color observation we find Δn to be constant for $\Delta V > V_{dis}$. Measurements at $\Delta V < V_{dis}$ yield slightly reduced and more irregular Δn consistent with the loss of homogeneity. In this condition birefringence has been taken as the average of various regions of the cell.

We performed SHG measurements on the same O3 cell using an optical setup built in-house (see Section 1 of Supporting Information and Fig. S1). The resulting data are also shown in Fig. 2a (green dots). We find the SHG intensity $I_{SHG}(\Delta V)$ to behave similarly to $\sigma_b(\Delta V)$: constant above V_{sat} and dropping to about half its large ΔV value at $V \approx V_{dis}$.

The combination of the three measurements shown in Fig. 2a indicates that the ordering of the N_F phase in planar parallel electrode cells can be split into three regimes:

- a large ΔV regime ($\Delta V > V_{sat}$, light blue shading), where the polar axis is uniformly oriented perpendicular to the electrodes, so that $\sigma_b = P$. In this regime, (i) $P = P_B$, where P_B is the bulk thermodynamic equilibrium value of P , repeatedly measured and reported in literature; (ii) P does not depend on ΔV (but only on T); (iii) the electric field experienced by the N_F phase is $E_{NF} = \Delta V_{NF}/d = (\Delta V - V_{sat})/d > 0$ and directed as P .
- an intermediate regime ($V_{dis} < \Delta V < V_{sat}$, pink shading) in which the nematic order - and thus the polar order - is perpendicular to the electrode, so that $\sigma_b = P$. Here, however, P has a reduced value ($P < P_B$) and it is proportional to the applied voltage ($P \propto \Delta V$) independently from the electrode separation, a finding that demonstrates the cancellation of the internal field ($E_{NF} = 0$, see discussion). In this regime the system modifies its effective polarization while preserving the nematic alignment. We define this behavior as ‘‘Polarization Plasticity’’.
- a low voltage regime ($\Delta V < V_{dis}$, gray shading) in which the director is still largely perpendicular to the electrodes (small decrease in birefringence), but macroscopic distortions are observed.

The observation of polarization plasticity in N_F raises the question of the micro or mesoscopic structuring enabling this behavior. One possible scenario is that of a microscopic reduction of the polar ordering, as if N_F was brought close to a $N_F - N$ phase transition. An alternative scenario is that the system splits into a mosaic of tubular domains with opposite polarity and $P = P_B$, separated by the nematic order-preserving walls, as sketched in Fig. 2c. In this scenario, the measured P results from the ratio of domains with positive and negative polarity.

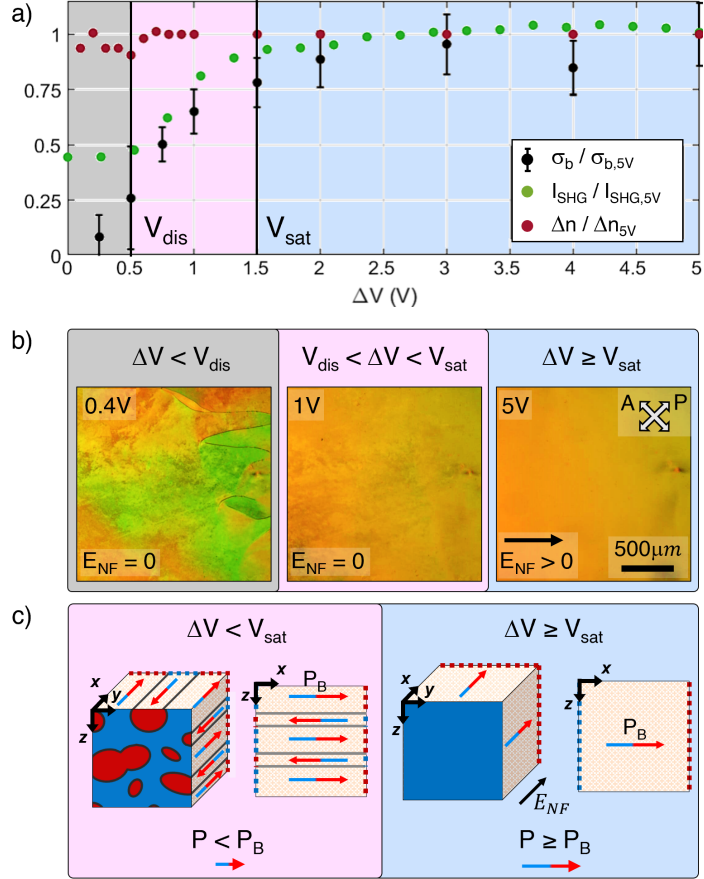


Figure 2. Optical characterization of the O3 cell a) Comparison of polarization charge density σ_b (generally coinciding with P , see text), SHG intensity I_{SHG} , and birefringence Δn as a function of ΔV . Each quantity is normalized over their values at $\Delta V = 5V$. Color shadings mark the three regimes of voltage described in the text. In pink the polarization plasticity range. b) PTOM images through cross polarizers P and A (white arrows) at different voltages. Black arrow: direction of the applied electric field E. c) Axonometric and lateral view of schematic representations of the polarization arrangement in N_F confined between electrodes with $\Delta V < V_{sat}$ and $\Delta V > V_{sat}$ (left and right hand side panel, respectively). Red and blue regions indicate surface of positive and negative bound charge accumulation, respectively. In the left hand side panel we sketch the proposed antipolar tubular domain structure that enables polarization plasticity.

Kinetics upon Voltage Reversal: Regimes of Charge Reversal

Additional information about the polarization plasticity is provided by the time dependence of the charge flow after voltage reversal that also indicate the presence of two regimes. Data from bulky cells show that for $\Delta V > V_{sat} \approx 3.7V$ (Fig. 3a) the $i(t)$ curves are bell shaped, with peak position and width that decrease with increasing voltage, in line with previous observations [1].

At lower voltages, ($\Delta V < V_{sat}$, Fig. 3b), the peak position of the $i(t)$ curves is weakly dependent on ΔV , with the whole shape changing with decreasing ΔV and becoming, for $\Delta V \leq 1V$, well described by exponential decays having a ΔV -independent decay time τ (see Fig. S2 in Section 2 of Supporting Information). In the case of the B4 cell (whose $i(t)$ are shown in the figure), $\tau = 24ms$. By interpreting

the exponential decays as RC discharge processes, and after having checked that τ does not depend on the probe R of the circuit, we determined the effective resistance $R_{eff} = \tau/C_{eff}$, based on the effective capacitance determined above.

Fig. 3c shows the values of R_{eff} for the family of bulky cells plotted as a function of the shape factor d/S . Since the dependence is nearly linear, from the slope (dashed line) we can determine the effective resistivity of the polar fluid during the reversal process $\rho_{NF} \approx 500\Omega \cdot m$. This value is close to the one obtained by dielectric spectroscopy measurements on DIO [15].

Kinetics upon Voltage Reversal: Comparison between Optical and Charge Switching Times

$i(t)$ measurements performed on the O1 cell, the thickest of the optical cells, confirm the same behavior observed in the B cells, although curves are noisier because of the much smaller S (see Table I). From $i(t)$ we extracted the discharging time τ_c , defined as the time after voltage reversal at which half of the flowing charge Q has flown in the circuit, which we plot in Fig. 3d (red dots) as a function of ΔV . In line with what observed above for the bulky cells, when $\Delta V \lesssim V_{sat}$, τ_c becomes weakly ΔV dependent and saturates to a constant value for $\Delta V \rightarrow 0$.

Since the O1 cell enables optical observations, we could study the time dependence of the transmitted intensity $I_T(t)$ as measured in bright field transmission microscopy (no polarizers) after voltage reversal, as in Ref. [5]. During such process $I_T(t)$ starts from an initial value $I_{T,0}$, it decreases to a minimum and it eventually grows back to $I_{T,0}$. The reduction of I_T reflects the disruption of the uniform nematic alignment into domains in which the polarization and the optical axis incoherently rotate toward the reversed direction. Such incoherent rotation gives rise to an optical inhomogeneous, and thus turbid, state which becomes again transparent when the rotation is completed and uniform alignment restored. From $I_T(t)$ we thus extracted τ_T , the delay after voltage reversal at which the largest turbidity - lowest I_T - is found. More details on τ_T calculation can be found in Section 3 of Supporting Information.

Fig. 3e and 3f compare $i(t)/i_{max}$ with $I_T(t)/I_{T,0}$ for respectively two choices of ΔV . For $\Delta V > V_{sat}$ (panel f), both curves are bell-shaped with comparable characteristic times, as also found in [1], while for $\Delta V < V_{sat}$ (panel e), τ_c is much shorter than τ_T . By comparing the two panels, it can also be noticed that the minimum of $I_T(t)/I_{T,0}$ is much more pronounced at large ΔV , indicating a larger turbidity.

A direct comparison between τ_T and τ_c measured in the O1 cell as a function of ΔV is shown in Fig. 3d. For large voltages the two curves collapse, both exhibiting a ΔV^{-1} trend (dashed black line). Conversely, by lowering ΔV below V_{sat} , the two trends differ, with τ_T maintaining the ΔV^{-1} dependence even at low ΔV . It is remarkable that in this regime we can find $\tau_c \approx 0.1\tau_T$, indicating that the fluid delivers a significant amount of charge much faster than the time it takes to resolve the optical disordering following voltage reversal.

The availability of a mechanism to transport bound charges between electrodes that does not generate optical turbidity becomes apparent when exploring sudden variations of ΔV between values of equal sign. When switching from ΔV_1 to ΔV_2 , both larger than V_{sat} , σ_b stays constant and no optical event is observed. Conversely, if $\Delta V_1 < V_{sat}$ and $\Delta V_2 > V_{sat}$, the transition from ΔV_1 to ΔV_2 involves bound charge displacement (from $\sigma_b = C_{eff}\Delta V_1/S$ to $\sigma_b = P$) but no observable turbidity. If instead the transition is from ΔV_2 to ΔV_1 , a global perturbation generating optical turbidity is observed, with features similar to those observed upon voltage reversal (see Fig. S4, in Section 4 of Supporting Information, for the case $\Delta V_1 = 0.5V$, $\Delta V_2 = 5V$).

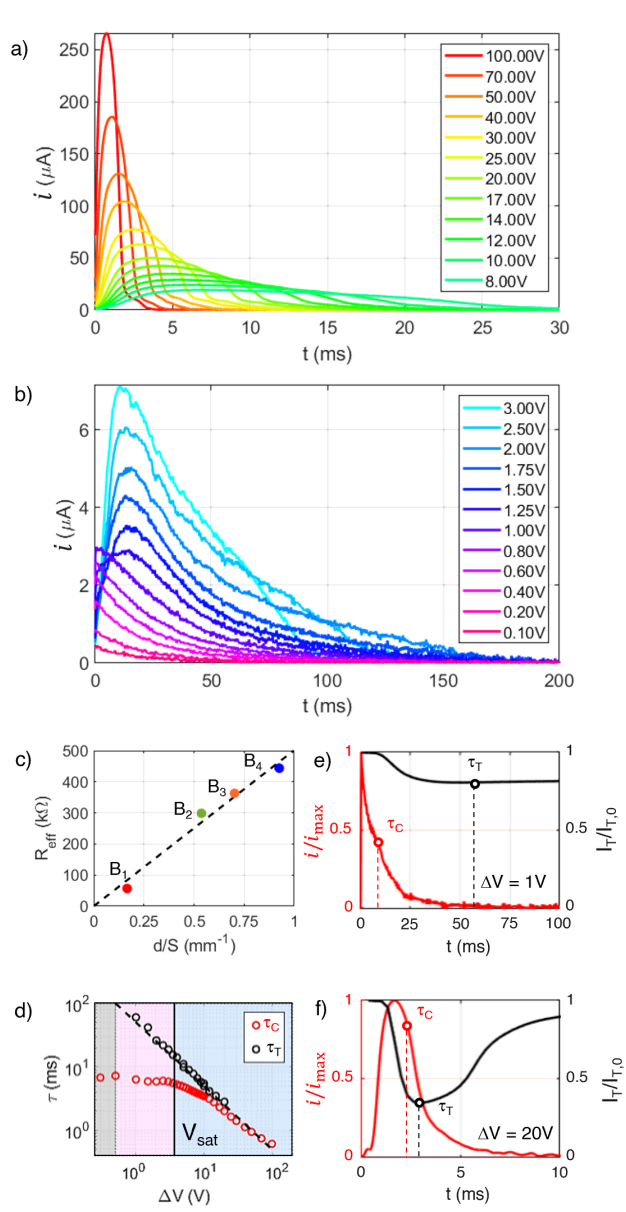


Figure 3. Kinetics upon voltage reversal a-b) $i(t)$ curves measured in the B4 cell with various voltages. c) Effective resistance R_{eff} determined from the exponential decay time τ in the bulky cell family, plotted against the shape factor d/S . Dashed line: linear fit. d) Discharge time τ_c (red dots) and optical response time τ_T (black dots) as a function of ΔV , in the O1 cell. Dashed line: ΔV^{-1} slope fit to the τ_T data. e-f) comparison of the current and optical transmission curves normalized to their largest value as a response to voltage reversal with $\Delta V = 1V$ and $\Delta V = 20V$, respectively.

Discussion

Equilibrium

We have found that for $\Delta V < V_{sat}$ all σ_b vs. ΔV data obtained in bulky cells with a wide range of electrode separation ($0.8mm - 4mm$) collapse on a common

$\sigma_b = \Delta V C_{eff}/S$ line (Fig. 1c). This finding demonstrates that voltage drop and electric field within the N_F fluid are negligible. In this condition the whole ΔV drop takes place at the electrodes, as previously suggested [12] (thick black line in Fig. 4a).

The reduction of P with respect to the bulk value P_B observed for $\Delta V < V_{sat}$ can be understood as the only available solution to avoid instability. Indeed, if P were to maintain its bulk value, the voltage drop across the N_F fluid would be $\Delta V - V_{sat} < 0$, and thus a field opposite to P would arise (yellow-to-red values in 4 a), leading to an unstable condition. Symmetrically, if a smaller P was present, a positive field (green-to-blue values) would promote its growth until the field is canceled. The condition of polarization plasticity can only be found when no electric field is present in the N_F .

The value $C_{eff}/S = 1.2\mu C/(V \cdot cm^2)$ extracted from bulky cell data refers to the two electrode capacitors in series, each of capacitance C_I . By treating these as planar capacitors, consisting of a dielectric layer of thickness δ_I and permittivity ε_I interposed between the N_F and the electrode, we obtain $C_I = 2C_{eff} = \varepsilon_I S/\delta_I$. If we take $\varepsilon_I \approx \varepsilon_0$ we find $\delta_I = 3.6\text{\AA}$, indicating that our observations are consistent with a very thin N_F -electrode separation (the molecule length is $\ell_{DIO} \approx 20\text{\AA}$), sufficiently thin to be compatible with the intrinsic disorder and/or staggering present in the fluid near the solid surface. Sensitivity to such a small interfacial gap reflects the distinctive properties of the N_F : a large bound-charge accumulation σ_b combined with fluidity and thus vanishing coercive field.

The value of V_{sat} depends on the electrode material: from the $P(\Delta V)$ curves in O2 and O3 cells, built with aluminum and ITO electrodes we obtain $V_{sat} = 10V$ and $V_{sat} = 1.5V$, respectively. The larger V_{sat} in O2 indicates a thicker insulating layer that we understand as a Al_2O_3 oxide layer whose typical thickness is of the order of 1-10 nm [18]. By considering an electrode gap formed by a 0.36nm-thick layer of vacuum (assumed to be general for N_F -solid surface interfaces) and by a layer of Al_2O_3 ($\varepsilon_{Al_2O_3} = 10\varepsilon_0$), we obtain a thickness $\delta_{Al_2O_3} = 6nm$. Interpreting the ITO cell is instead made difficult by the different geometry, with flat surface-bound electrode.

When $\Delta V \geq V_{sat}$, $P = P_B$ and the voltage drop in N_F is $\Delta V_{N_F} = \Delta V - V_{sat}$ (thick line, Fig. 4b). Thus,

$$P(\Delta V) = \begin{cases} P_B & \Delta V \geq V_{sat} \\ \frac{\Delta V}{V_{sat}} P_B = \frac{\varepsilon_I}{2\delta_I} \Delta V & \Delta V \leq V_{sat}. \end{cases} \quad (1a)$$

$$(1b)$$

The observation that a condition of reduced σ_b is not obtained through a rotation of the polar order - which would lead a charge accumulation on the side walls generating an opposing field - but via a polarization reduction of a well aligned nematic with $P < P_B$ (Eq. 1b) is the core finding of this work. This condition of polar plasticity can only be obtained by inverting a fraction of the molecules while maintaining their nematic order. An unavoidable question is on which length scales such inverted molecules are polarly correlated. One possibility is that the correlations are very short, with molecular lengths, which would correspond to a uniform loss of polar order parameter as if approaching a transition toward a conventional nematic. This scenario appears however energetically unfavorable since uniform nematization would require to overcome the thermodynamic free energy associated to polar order, an estimate of which is the latent heat of the polar-apolar transition, $\sim 100J/kg$ [19]. This value should be compared with the electrostatic energy density $P_B \cdot V_{sat}/d \sim 0.1J/kg$, a much smaller quantity. Furthermore, a transition toward a conventional (non-polar) nematic typically brings a significant drop in birefringence [20], which we do not observe.

A more realistic alternative is that the polar correlation extend on the mesoscale, giving rise to a splitting of the system into tube-shaped domains having local

polarization P_B reversed polarity. We sketched such ‘‘Antipolar Tubular Domains’’ (ATD) scenario in Fig. 2c. With respect to the uniform reduction of P , in which the largest majority of the molecules would be involved in antipolar interactions, the ATD structure has the advantage of reducing the antipolar interface and thus the associated energy cost. Also, because of the electrode-to-electrode tubular structure, the charges accumulating on the bases are compensated by the free positioning of the charges on the electrodes.

While the combination of reduced P and unmodified optical axis and birefringence demonstrates polarization plasticity, no optical feature indicating inter-domain walls is observed. We interpret this feature as an evidence that the interface between ATD and Pure Polarization Reversal walls observed in N_F between domains of opposite polarity [4], and in other polar phases such as in SmA_F [21], in splay nematic antiferroelectric [22] and in SmZ_A phases [23]. Indeed, in the need to escape frustration, the system might drift toward antiferroelectric-like structures, which are closer to the N_F phase than the apolar nematic phase [23].

Polarity Reversal

In the PCG relaxation mode approach, the polarity reversal takes place through a coherent rotation of the polarization, resulting in symmetric bell shaped $i(t)$ with peak time $t_p \sim P_b \rho_{N_F} d / \Delta V$, as shown in Section 5_b of Supporting Information. This result, obtained for $\Delta V \gg V_{sat}$, is in semi-quantitative agreement with the observed $i(t)$ in the large voltage regime (Fig. 3a), where inversion takes place through splitting in mesoscopic domains undergoing rotations and where $\tau \propto \Delta V^{-1}$ (Fig. 3d).

When $\Delta V < V_{sat}$, a second distinct polarization reversal mode becomes active, as indicated by: (i) the change in the shape of the current curves that cross-over from a bell-shaped to a decaying exponential response (Fig. 3b); (ii) the separation between τ_c and τ_T , with the former deviating from the ΔV^{-1} scaling (Fig. 3d); (iii) the decreased turbidity with a very slow recovery at small ΔV (Fig. 3e and Fig. S4). Being this second reversal mode appearing together with the polar plasticity of N_F , it is reasonable to assume that these phenomena are intimately connected.

The Antipolar Tubular Domains structure described above enables an alternative polarization reversal mechanism. In the ATD structure, the average polarization P is determined by the fraction x of the system with ‘‘positive’’ (arbitrarily chosen) polarity: $P(x) = +xP_B + (1-x)(-P_B) = (2x-1)P_B$. At equilibrium, $x_{eq} = 1/2 + \Delta V/2V_{sat}$. Thus, in the polarization plasticity regime, changes in P can occur via the motion of the domain walls.

Fig. 4c and d sketch the process of polarization inversion via domain wall displacement. After voltage reversal, the previous equilibrium state becomes unstable and the system undergoes a transformation $x_{eq} \rightarrow 1 - x_{eq}$.

As the walls move, a change δx in the fractional polarity is produced with a corresponding variation of electrostatic energy $\delta U = -2P_B E_{N_F} v \delta x$, where $v = hwd$ is the cell volume (see Fig. 4 c). Thus, the force per unit length acting to bring the walls to the equilibrium position is:

$$F(x) = -\frac{\delta U}{S \delta x} = -4P_B V_{sat} (x - x_{eq}), \quad (2)$$

where S is the electrode surface ($S = hw$). The wall motion will be determined by the balance of such force with the contrasting viscosity: $F(x) = -\eta \dot{x}$, where η has the dimension of a surface viscosity.

The very same process determines the current of polarization charges:

$$i = 2P_b S \dot{x} = \frac{\Delta V_{N_F}}{R_{eff}}, \quad (3)$$

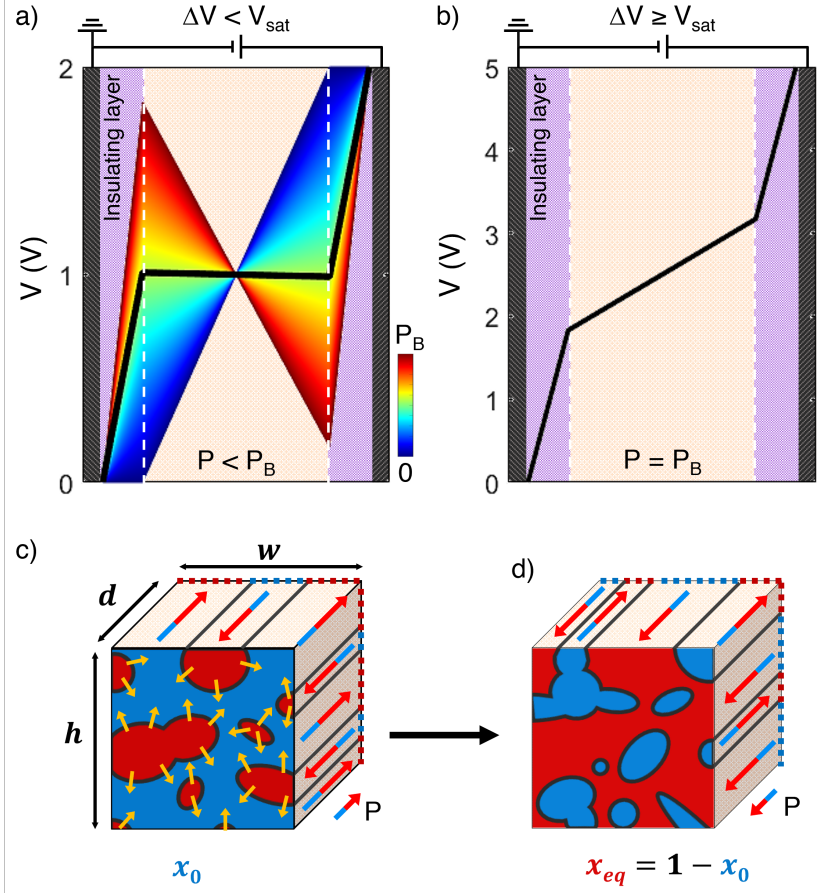


Figure 4. Electrostatics and structure in the polarization plasticity state a-b) Thick black line: voltage at equilibrium as a function of the distance from the grounded electrode for $\Delta V < V_{sat}$ (a) $\Delta V \geq V_{sat}$ (b). Colors in (a) indicate the voltage profile across the cell that would be present if P was larger (yellow to red) or smaller (green to blue) than its equilibrium value. c-d) same sketch of the Antipolar Tubular Domain structure as in Fig. 2c. Yellow arrows indicate the motion of the domain walls by which the minority fraction (red) expands to reverse the sign of P , as in the transition following voltage reversal.

where R_{eff} the effective resistance defined above Eq.3 maps into the force balance equation provided that $\eta = 4P_B^2 d \rho_{N_F}$. The quantity $P^2 \rho_{N_F}$ is a rotational viscosity [13].

By choosing as initial condition $x_0 = 1 - x_{eq}$, as in a voltage reversal experiment, we obtain:

$$x(t) = \frac{1}{2} + \frac{\Delta V}{2V_{sat}} - \frac{\Delta V}{V_{sat}} \exp\left(-\frac{t}{R_{eff} C_{eff}}\right). \quad (4)$$

Thus, the wall dynamics leads to exponentially decaying currents with characteristic time $R_{eff} C_{eff}$, which agrees with the basic features of the observed additional route for polarization inversion, exponential in shape (Fig. 3b and Fig. S2 in Section 2 of Supporting Information) and with a ΔV -independent characteristic time (Fig. 3d).

Thus, while at $\Delta V > V_{sat}$ the polarization inverts through optically detectable rotations taking place in a $t_p \sim \Delta V^{-1}$ time common to optical and electric inversion signatures, at $\Delta V < V_{sat}$ the situation is richer. According to our proposed ATD model, the system becomes divided in domains of opposite polarities, a situation that makes it

possible for both mechanism of polarity inversion to be active: the optically undetectable wall displacement yielding exponential decaying current, and the optically detectable rotation of portions of the domains that are directed opposite to the field. Indeed, the presence of a $\sim \Delta V^{-1}$ decaying mode is by itself an indication that there are portions of the sample where the local polarization is P_B and opposite to the field, so that their inversion time by rotation scales with continuity to the $\Delta V > V_{sat}$ behavior.

A strong confirmation of the polarization changes via domain expansion/contraction is given by the response to asymmetric switches described above (Fig. S3, in Section 3 of Supporting Information): P variations via wall displacement is possible when the starting conditions of the system is to be split in ATD (as in $\Delta V_1 = 0.5V$ to $\Delta V_2 = 5V$ switches) but not when the system is initially uniformly polarized with $P = P_B$ (as in $\Delta V_2 = 5V$ to $\Delta V_1 = 0.5V$ switches). In this latter condition the system thus responds by breaking in domains that undergo rotation.

Conclusion

In this work we have explored the behavior of a ferroelectric nematic fluid in a seemingly straightforward condition: between parallel planar electrodes at low voltage. By comparing the behavior of bulky cells with various electrode distance we have shown that there is a threshold voltage V_{sat} (already reported in previous works [10, 13]) at which the N_F polarization is at its bulk value P_B and the applied voltage entirely falls at the electrodes because of their intrinsic capacitance. When the voltage applied to the cells is below that threshold, the system becomes frustrated, unable to maintain its bulk polarization while avoiding depolarization fields. We find that in this condition, the N_F phase enters a different state, as testified by equilibrium and dynamic, electric and optical observations. In such a state, the ferroelectric fluid maintains the nematic ordering with unmodified birefringence and no sign of disordering into domains (except at very low voltages) while effectively lowering its average bulk polarization. We have found that in such state, that we have dubbed of ‘‘Polarization Plasticity’’, the system modifies not only its polarization but also its kinetic response to electric field variation, with the appearance of a route for polarization inversion faster than $\sim \Delta V^{-1}$.

We argue that the structure most compatible with the data is that of a system divided into tubular domains of opposite polarity, which we define as ‘‘Antipolar Tubular Domains’’ model, separated by pure polarization reversal walls. Indeed, such a structure combines: (i) the tendency of N_F materials to develop, in contiguous phases walls separating domains of opposite polarities as in the Smectic A_F or splay-nematic phase [21–24]; (ii) the local polarizability equal to the bulk P_B , a condition that minimizes energy costs and is coherent with the observation of a remnant $\sim \Delta V^{-1}$ decay time; (iii) the availability of an additional degree of freedom - the motion of domain wall - that gives rise to an alternative switching process that has no optical signature.

The polarization plasticity state is peculiar to ferroelectric nematics, with no counterpart in ferroic solid materials in which the coupling of P to the crystallographic direction enables the formation of history-dependent ordering, such as the one intentionally produced by poling. Polarization plasticity, here demonstrated for a simple configuration, could actually be the general strategy for N_F phases to avoid electrostatic instability in a much wider set of frustrated conditions, including defect, domain walls and splay-inducing boundary conditions. This state, and the associated exponential relaxation upon voltage reversal, could also come into play in the design of applications of N_F for fast-charging processes in energy storage.

Cell preparation

Bulky cells are constructed using two stainless steel plates as electrodes, separated by a silicone sheet acting both as a spacer and gasket. The sheet contains a precut mask defining the measurement volume, with the top side open for material insertion. DIO is loaded in the solid phase, heated in an oven at $T = 140^\circ\text{C}$ for the minimum time required to melt into the N phase, and quickly cooled in the N_F at $T = 60^\circ\text{C}$, where experiments are conducted. The distance between the electrodes d , as well as the height h and the width w of the mask are measured with an electronic caliber. The actual filling of the cell has been verified by measuring the DIO mass m after the experiment and computing the volume $v = m/\rho_{DIO}$, where $\rho_{DIO} = 1.3\text{g/cm}^3$ [25].

IPS optical thin cells with metallic electrodes are produced using two stainless steel or aluminum foil strips as both electrodes and spacers between two optical glasses. Instead, cells with ITO electrodes are produced by sandwiching two Mylar film spacers between an optical glass slab and an ITO-coated glass slide, from which the electrodes and the optical region are etched. The etching is obtained by masking the electrode regions with silicone pads and depositing a small volume of a 50% v/v solution of H_2SO_4 in H_2O on the exposed area. The slide is then heated on a hot stage at $T = 80^\circ\text{C}$ for 5 minutes, carefully washed with H_2O and air dried. For every thin cell, glass surfaces are treated with hexadecyltrimethoxysilane (HDTMS) and left unrubbed to favor a degenerate planar alignment [26]. Silanization is performed by stirring a 2% v/v solution of HDTMS in a 95:5 ethanol-water mixture, acidified to pH 5 with acetic acid, for 5 minutes at room temperature. The solution is then pipetted onto the slides and, after solvent evaporation, the slides are heated on a hot plate at $T = 110^\circ\text{C}$ for 10 minutes and stored at room temperature over night. The slides are eventually rinsed with isopropanol to remove the excess of silane. Cells are assembled with metallic clips and the thickness is measured via Fabry-Perot interferometry technique. DIO is finally loaded by capillarity in the N phase at $T = 140^\circ\text{C}$ and immediately cooled in the N_F phase at $T = 60^\circ\text{C}$.

Acknowledgments

The authors would like to thank Prof. Noel Clark for precious discussions. S. M. and F. C. acknowledge support by Fondazione Cariplo, grant Young Researcher no. 2023-1095. R.J.M thanks UKRI for funding via a Future Leaders Fellowship, grant number MR/W006391/1, and the University of Leeds for funding via a University Academic Fellowship. R.J.M. gratefully acknowledges support from Merck KGaA.

Supporting Information

The present Supporting Information is composed as follows:

- Section 1: SHG measurement setup and Figure S1;
- Section 2: RC relaxation curves at low voltages and Figure S2;
- Section 3 τ_T extraction from the transmitted intensity curves and Figure S4;
- Section 4: Response to asymmetric voltage switches and Figure S3;
- Section 5: Derivation of the kinetic behavior from the PCG model reorientation mode.

SI Section 1: SHG measurement

SHG measurements were performed with a custom-made optical setup (Fig. S1), consisting of a Nd:YAG pulsed laser (pulse duration 10ns, repetition rate 10Hz) at $\lambda = 1064nm$ impinging perpendicularly on the optical cells polarized along the N_F director by a Glan-Laser polarizer. The second harmonic signal is collected through a second polarizer parallel to the first and analyzed with a Ocean USB2000+ spectrometer to selectively measure the intensity of the $\lambda = 532nm$ peak, rejecting stray light and possibly minimizing power leakages from the carrier wavelength. The integrated SHG peak was measured at various ΔV to obtain $I_{SHG}(\Delta V)$. For every voltage, measurements were repeated in over 20 zones around the sample and then averaged.

The detected I_{SHG} signal is, by definition [27], the result of the chosen experimental conditions: (i) is a tensorial quantity as it depends on the polarization of the input photons, which summed up create the doubled frequency, and of course from the final polarization analyzed; (ii) it changes periodically with the optical path length as it suffers from the phase matching of the second harmonic signal and the carrier wavelength. To avoid introducing artifacts due to (i) and (ii) we performed SHG measurements on the same thin optical cells we used for charge/optical measurements (the thickness was kept constant) and we employed glan-laser polarizers to carefully control both the input and the output optical polarization to be parallel to the liquid crystal director of N_F

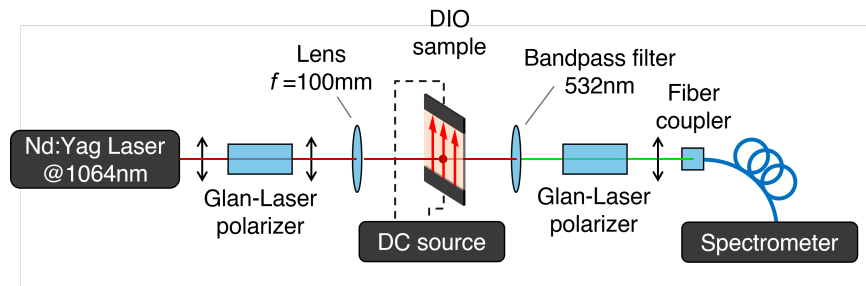


Figure S1. SHG measurement setup Schematic representation of the custom SHG intensity measurements setup used in this work.

SI Section 2: RC relaxation curves at low voltages

At low voltages the $i(t)$ curves exhibit an exponential decay typical of RC relaxation processes. In Fig. S2, we show the $i(t)/\Delta V$ curves in the B4 cell at low voltages (colored lines). From such curves, we obtain an average curve (black line), that is well fitted with an exponential decay (yellow dashed curve).

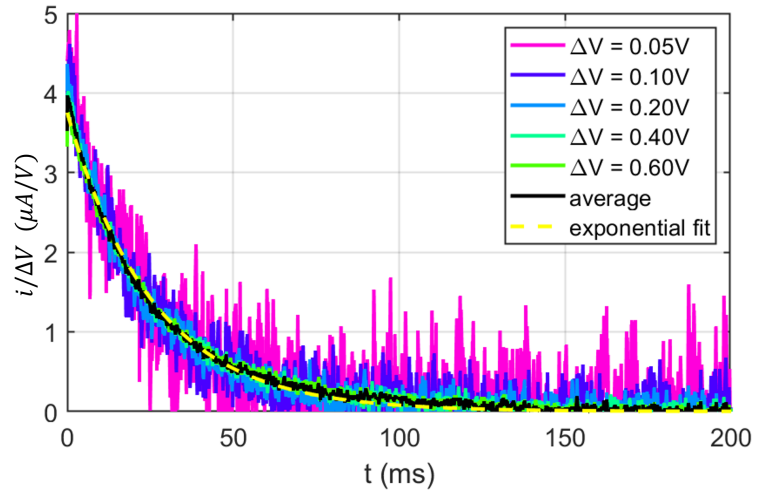


Figure S2. Current intensity $i(t)$ at low voltages (colored solid curves), normalized on ΔV in the B4 cell. In black the weighted average of the curves, fitted with an exponential decay (dashed yellow line).

SI Section 3: Response to asymmetric voltage switches

To better understand the behavior of the polar fluid during domain expansion/contraction we studied the response to asymmetric switches: the most emblematic case of voltage switches from $0.5V$ to $5V$ and vice-versa is reported in Fig. S3, with the transmitted intensity curves and snapshots of the processes. From $0.5V$ to $5V$ there is not significant perturbation of the fluid, whereas from $5V$ to $0.5V$ the system responds by breaking in domains that undergo rotation.

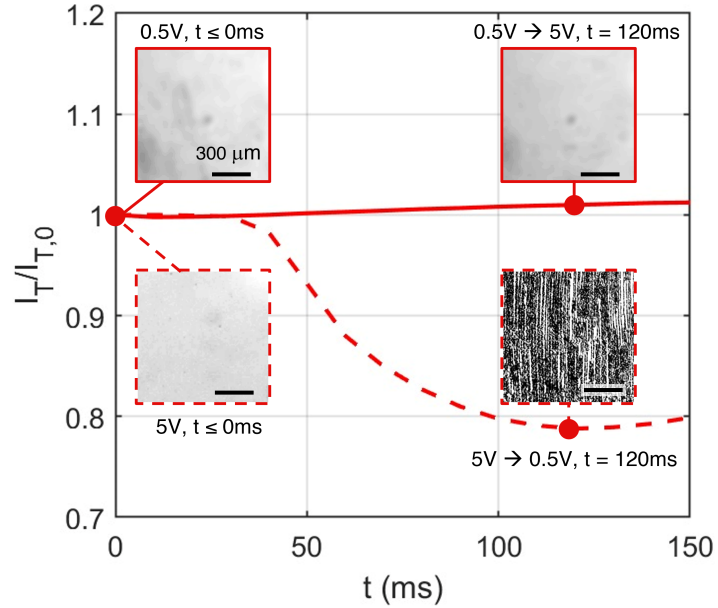


Figure S3. Transmitted intensity I_T measurements after voltage change across V_{sat} , in the O3 cell. Solid line: I_T after the voltage change from $0.5V$ to $5V$; dashed line: I_T after the voltage change from $5V$ to $0.5V$. Pictures represent frame of the two measurements, in equilibrium before the switch and at $t = 120ms$, wherein I_T reaches its minimum value in the $5V$ to $0.5V$ measurement.

SI Section 4: τ_T extraction

The response to voltage reversal results in a reconfiguration of the polar alignment: the homogeneous N_F medium becomes turbid decreasing the bright field transmitted intensity I_T and then recovers the polar order, coming back to the initial transmitted intensity $I_{T,0}$. We measured I_T with a Teledyne Prime BSI Express camera at 3030 fps, which has been synchronized with a National Instrument PCIe-6323 multifunctional I/O card as voltage source to properly identify and image the voltage reversal moment. After computing I_T as the average signal in the ROI, we obtain maximum turbidity time τ_T as the moment after the voltage reversal in which I_T reaches its minimum value. In Fig. S4 the normalized bright field transmission intensity curves $I_T(t)$ after the voltage reversal are shown, together with τ_T .

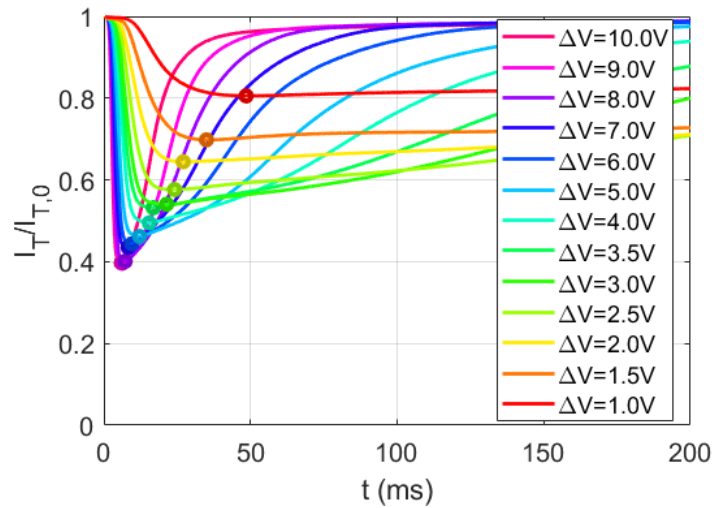


Figure S4. τ_T measurement Normalized I_T transmission intensity curves after the voltage reversal, in the O1 cell. τ_T is obtained as the time of minimum intensity (dots), for each voltage.

SI Section 5: Derivation of the kinetic behavior from the PCG model

Following the PC-Goldstone model from Clark et al. [13], we can discuss the re-orientation process of the polar fluid depending on the angle ϕ between \vec{P} and \vec{E}_{NF} . We can write the temporal evolution of ϕ as follows:

$$\begin{aligned}\frac{d\phi}{dt} &= \frac{1}{\gamma} P E_{NF} \cdot \sin(\phi) = -\frac{P V_{NF}}{\gamma d} \sin(\phi) = \\ &= -\frac{P}{\gamma d} (\Delta V - \cos(\phi) V_{sat}) \sin(\phi) = \\ &= -\left[\tau_{high}^{-1} - \cos(\phi) \tau_{low}^{-1} \right] \sin(\phi),\end{aligned}\tag{5}$$

wherein we exploited that ΔV is constant during the reversal process, since we have a squared voltage wave, whereas in [13] a triangular wave is considered. Two characteristic times are defined as $\tau_{low} = \frac{\gamma d}{P V_{sat}}$ and $\tau_{high} = \frac{\gamma d}{P \Delta V}$, depending on the rotational viscosity γ .

a) Derivation at low voltages

For $\Delta V \ll V_{sat}$, in the Clark et al. model [13], the reversal is considered at angles $\phi \approx \pi/2$. Solving the problem for $\psi = \phi - \pi/2 \approx 0$, and thus $\sin(\psi) \approx \psi$ and $\sin(\phi) \approx 1$, the Eq. 5 can be written as follows:

$$\dot{\psi} \approx -\tau_{high}^{-1} - \psi \cdot \tau_{low}^{-1},\tag{6}$$

which is a first-order linear ordinary differential equation. The solution is the following:

$$\psi(t) = k e^{-t/\tau_{low}} - \frac{\tau_{low}}{\tau_{high}} = k e^{-t/\tau_{low}} - \frac{\Delta V}{V_{sat}},\tag{7}$$

meaning that we have an exponential relaxation, with characteristic time τ_{low} , to an equilibrium condition $\psi(t) = -\frac{\Delta V}{V_{sat}}$. k is determined by the initial condition of the problem $\psi(t=0)$. Also the polarization P_z faced to the electrode as the same exponential behavior:

$$\frac{P_z(t)}{P} = \cos(\phi(t)) = -\sin(\psi(t)) \approx -k e^{-t/\tau_{low}} + \frac{\Delta V}{V_{sat}},\tag{8}$$

whose equilibration as $P_z(t)/P = \Delta V/V_{sat}$ satisfies the $E_{NF} = 0$ condition for $\Delta V < V_{sat}$.

We can also calculate the current intensity in the polarization reversal process as follows:

$$\frac{I(t)}{PS} = \frac{1}{P} \frac{dP_z}{dt} = +\frac{k}{\tau_{low}} e^{-t/\tau_{low}},\tag{9}$$

that is again an exponential decay with characteristic time τ_{low} . This quantity can be referred to the resistivity as $\tau_{low} = \frac{\gamma d}{P V_{sat}} = \frac{\rho_{NF} \cdot P d}{V_{sat}} = R_{eff} \cdot C_{eff}$, which is the same found in our model for the PPR wall motion.

b) Derivation at high voltages

For $\Delta V \gg V_{sat}$, i.e., $\tau_{high}^{-1} \gg \tau_{low}^{-1}$, the Eq. 5 can be written as follows:

$$\dot{\phi} \approx -\tau_{high}^{-1} \sin(\phi), \quad (10)$$

which is a first-order nonlinear ordinary differential equation, whose solution is the following:

$$\phi(t) = 2\cot^{-1}(e^{k+t/\tau_{high}}), \quad (11)$$

wherein $\cot^{-1}(x)$ is the inverse of the cotangent function and k is determined by the initial condition $\phi(t=0)$. Starting from $\phi(t=0) \approx \pi$, $\phi(t)$ exhibits a smooth transition to $\phi \approx 0$ for long times, similarly to a sigmoidal trend. The resulting $P_z(t) = P \cos(\phi(t))$ goes from $-P$ to P , and we can find the expression of the current intensity:

$$\frac{I(t)}{PS} = \frac{1}{P} \frac{dP_Z}{dt} = \frac{2e^{k+t/\tau_{high}} \cdot \sin[2\cot^{-1}(e^{k+t/\tau_{high}})]}{\tau_{high}[e^{2(k+t/\tau_{high})} + 1]}, \quad (12)$$

that is a symmetric bell shape with peak at $t = k \cdot \tau_{high} = k \frac{\rho_{NF} \cdot Pd}{\Delta V}$, which scales linearly with ΔV^{-1} .

References

1. Xi Chen, Eva Korblova, Dengpan Dong, Xiaoyu Wei, Renfan Shao, Leo Radzihovsky, Matthew A. Glaser, Joseph E. Maclennan, Dmitry Bedrov, David M. Walba, and Noel A. Clark. First-principles experimental demonstration of ferroelectricity in a thermotropic nematic liquid crystal: Polar domains and striking electro-optics. *Proceedings of the National Academy of Sciences*, 117(25):14021–14031, June 2020.
2. Hiroya Nishikawa, Kazuya Shiroshita, Hiroki Higuchi, Yasushi Okumura, Yasuhiro Haseba, Shin-ichi Yamamoto, Koki Sago, and Hirotsugu Kikuchi. A fluid liquid-crystal material with highly polar order. *Advanced Materials*, 29(43), October 2017.
3. Richard J. Mandle, S. J. Cowling, and J. W. Goodby. A nematic to nematic transformation exhibited by a rod-like liquid crystal. *Physical Chemistry Chemical Physics*, 19(18):11429–11435, 2017.
4. Oleg D. Lavrentovich. Ferroelectric nematic liquid crystal, a century in waiting. *Proceedings of the National Academy of Sciences*, 117(26):14629–14631, June 2020.
5. Federico Caimi, Giovanni Nava, Susanna Fuschetto, Liana Lucchetti, Petra Paiè, Roberto Osellame, Xi Chen, Noel A. Clark, Matthew A. Glaser, and Tommaso Bellini. Fluid superscreening and polarization following in confined ferroelectric nematics. *Nature Physics*, 19(11):1658–1666, July 2023.
6. Bijaya Basnet, Mojtaba Rajabi, Hao Wang, Priyanka Kumari, Kamal Thapa, Sanjoy Paul, Maxim O. Lavrentovich, and Oleg D. Lavrentovich. Soliton walls paired by polar surface interactions in a ferroelectric nematic liquid crystal. *Nature Communications*, 13(1), July 2022.
7. Stefano Marni, Federico Caimi, Raouf Barboza, Noel Clark, Tommaso Bellini, and Liana Lucchetti. Fluid jets and polar domains, on the relationship between electromechanical instability and topology in ferroelectric nematic liquid crystal droplets. *Soft Matter*, 20(25):4878–4885, 2024.

-
8. Maxim O. Lavrentovich, Priyanka Kumari, and Oleg D. Lavrentovich. Twist, splay, and uniform domains in ferroelectric nematic liquid crystals. *Nature Communications*, 16(1), July 2025.
 9. Alexander Jarosik, Hajnalka Nádasi, Michael Schwidder, Atsutaka Manabe, Matthias Bremer, Melanie Klasen-Memmer, and Alexey Eremin. Fluid fibers in true 3d ferroelectric liquids. *Proceedings of the National Academy of Sciences*, 121(13), March 2024.
 10. Diana Nikolova, Rachel Tuffin, Helen F. Gleeson, and Mikhail Osipov. Thermodynamic potential of ferroelectric nematic liquid crystals and consequences for polarization switching. *Physical Review E*, 112(1), July 2025.
 11. Natalia Podoliak, Lubor Lejček, Martin Cigl, and Vladimíra Novotná. Tunable defect patterns induced by a low-frequency electric field in ferroelectric nematic liquid crystals. *Soft Matter*, 2025.
 12. N. A. Clark, D. Coleman, and J. E. MacLennan. Electrostatics and the electro-optic behaviour of chiral smectics c: “block” polarization screening of applied voltage and “v-shaped” switching. *Liquid Crystals*, 27(7):985–990, July 2000.
 13. Noel A. Clark, Xi Chen, Joseph E. MacLennan, and Matthew A. Glaser. Dielectric spectroscopy of ferroelectric nematic liquid crystals: Measuring the capacitance of insulating interfacial layers. *Physical Review Research*, 6(1), February 2024.
 14. Alex Adaka, Mojtaba Rajabi, Nilanthi Haputhantrige, Samuel Sprunt, Oleg D. Lavrentovich, and Antal Jákli. Dielectric properties of a ferroelectric nematic material: Quantitative test of the polarization-capacitance goldstone mode. *Physical Review Letters*, 133(3), July 2024.
 15. A. Erkoreka and J. Martinez-Perdiguero. Constraining the value of the dielectric constant of the ferroelectric nematic phase. *Physical Review E*, 110(2):L022701, 2024.
 16. Netra Prasad Dhakal, Alex Adaka, Robert J. Twieg, Noel A. Clark, and Antal Jákli. Transient negative capacitance in ferroelectric nematic liquid crystals. *Physical Review Applied*, 24(1), July 2025.
 17. Jordan Hobbs, Calum J. Gibb, and Richard J. Mandle. Emergent antiferroelectric ordering and the coupling of liquid crystalline and polar order. *Small Science*, 4(10):2400189, 2024.
 18. L.P.H. Jeurgens, W.G. Sloof, F.D. Tichelaar, C.G. Borsboom, and E.J. Mittemeijer. Determination of thickness and composition of aluminium-oxide overlayers on aluminium substrates. *Applied Surface Science*, 144–145:11–15, April 1999.
 19. J. Thoen, G. Cordoyiannis, E. Korblova, D. M. Walba, N. A. Clark, W. Jiang, G. H. Mehl, and C. Glorieux. Calorimetric evidence for the existence of an intermediate phase between the ferroelectric nematic phase and the nematic phase in the liquid crystal rm734. *Physical Review E*, 110(1), July 2024.
 20. Stevie Brown, Ewan Cruickshank, John M. D. Storey, Corrie T. Imrie, Damian Pocięcha, Magdalena Majewska, Anna Makal, and Ewa Gorecka. Multiple polar and non-polar nematic phases. *ChemPhysChem*, 22(24):2506–2510, November 2021.

-
21. Xi Chen, Vikina Martinez, Pierre Nacke, Eva Korblova, Atsutaka Manabe, Melanie Klasen-Memmer, Guillaume Freychet, Mikhail Zhernenkov, Matthew A. Glaser, Leo Radzihovsky, Joseph E. MacLennan, David M. Walba, Matthias Bremer, Frank Giesselmann, and Noel A. Clark. Observation of a uniaxial ferroelectric smectic a phase. *Proceedings of the National Academy of Sciences*, 119(47), November 2022.
 22. Nerea Sebastián, Martin Čopič, and Alenka Mertelj. Ferroelectric nematic liquid-crystalline phases. *Physical Review E*, 106(2), August 2022.
 23. Xi Chen, Vikina Martinez, Eva Korblova, Guillaume Freychet, Mikhail Zhernenkov, Matthew A. Glaser, Cheng Wang, Chenhui Zhu, Leo Radzihovsky, Joseph E. MacLennan, David M. Walba, and Noel A. Clark. The smectic z a phase: Antiferroelectric smectic order as a prelude to the ferroelectric nematic. *Proceedings of the National Academy of Sciences*, 120(8), February 2023.
 24. Peter Medle Rupnik, Ema Hanžel, Matija Lovšin, Natan Osterman, Calum Jordan Gibb, Richard J. Mandle, Nerea Sebastián, and Alenka Mertelj. Antiferroelectric order in nematic liquids: Flexoelectricity versus electrostatics. *Advanced Science*, 12(9):2414818, 2025.
 25. C. Parton-Barr, H. F. Gleeson, and R. J. Mandle. Room-temperature ferroelectric nematic liquid crystal showing a large and diverging density. *Soft Matter*, 20(3):672–680, 2024.
 26. Federico Caimi, Giovanni Nava, Raouf Barboza, Noel A. Clark, Eva Korblova, David M. Walba, Tommaso Bellini, and Liana Lucchetti. Surface alignment of ferroelectric nematic liquid crystals. *Soft Matter*, 17:8130–8139, 2021.
 27. Orazio Svelto. *Principles of Lasers - 5th edition - pp.517-524*. Springer US, 2010.